



Research Article

Speckle Noise Removal by Energy Models with New Regularization Setting

Bo Chen ^{1,2}, Jinbin Zou,¹ and Weiqiang Zhang ¹

¹Shenzhen Key Laboratory of Advanced Machine Learning and Applications, College of Mathematics and Statistics, Shenzhen University, Shenzhen 518060, China

²Guangdong Key Laboratory of Intelligent Information Processing, Shenzhen University, Shenzhen 518060, China

Correspondence should be addressed to Bo Chen; chenbo@szu.edu.cn and Weiqiang Zhang; wqzhang@szu.edu.cn

Received 26 April 2020; Accepted 17 June 2020; Published 20 July 2020

Guest Editor: Yuanfang Ru

Copyright © 2020 Bo Chen et al. This is an open access article distributed under the Creative Commons Attribution License, which permits unrestricted use, distribution, and reproduction in any medium, provided the original work is properly cited.

In this paper, we introduce two novel total variation models to deal with speckle noise in ultrasound image in order to retain the fine details more effectively and to improve the speed of energy diffusion during the process. Firstly, two new convex functions are introduced as regularization term in the adaptive total variation model, and then, the diffusion performances of Hypersurface Total Variation (HYPTV) model and Logarithmic Total Variation (LOGTV) model are analyzed mathematically through the physical characteristics of local coordinates. We have shown that the larger positive parameter in the model is set, the greater energy diffusion speed appears to be, but it will cause the image to be too smooth that required adequate attention. Numerical experimental results show that our proposed LOGTV model for speckle noise removal is superior to traditional models, not only in visual effect but also in quantitative measures.

1. Introduction

With the development of digital image technology, a large number of digital images are transmitted and compressed through various channels. However, image corruption usually is unavoidable during transmission and storage, and the resultant noise quite often seriously affects the visual effect of the image. Clearly, high-quality images are desirable in many areas, such as in medical imaging and pattern recognition. Thus, image denoising is a critical step in image processing and computer vision, which plays an important role in various applied areas, especially in medical imaging, video processing, and remote sensing. On the other hand, it is also an important preprocessing process for other image processing that relies on subsequent processing.

Today, image denoising becomes research of focus, and many image denoising methods have been proposed such as Lee filter [1], Kuan filter [2], locally adaptive statistic filters [3–5], PDE-based and curvature-based methods [6, 7], wavelet transform based thresholding methods [8], and total vari-

ational [9–11]. In addition, the method based on machine learning [12–15] has received wide attention in recent years, such as deep learning [12, 13], linear regression [14], and Bayesian learning [13, 15].

In 1992, Rudin et al. [10] proposed a denoising model based on the total variation:

$$E_{\lambda_1}(u) = \int_{\Omega} |Du| dx + \frac{\lambda_1}{2} \int_{\Omega} |u - u^0|^2 dx, \quad (1)$$

where $\int_{\Omega} |Du| dx = \sup \{ \int_{\Omega} u \operatorname{div}(\varphi) \mid \varphi \in C_c^1(\Omega, \mathbb{R}^n), \|\varphi\|_{\infty} \leq 1 \}$ represents the TV regularization term, $u : \Omega \rightarrow \mathbb{R}$ is an original image that is without noise, $u^0 = u + n$ is noisy image, and n represents the Gaussian random noise with mean zero and standard deviation σ . $\lambda_1 > 0$ represents the regularization parameter which can be used to balance the fidelity terms and regularized terms in TV model, and $|Du|$ represents the L^1 norm of the image gradient.

It is well known that medical ultrasonic images may have many noises of speckle, which will bring a significant problem in terms of the quality of ultrasonic images and cover up the lesions of certain important tissues. Further, it brings great difficulties to the accurate diagnosis and identification of certain specific diseases and can create the potential risk of missed diagnosis and misdiagnosis. Thus, it is very desirable to eliminate the speckle noise in ultrasound image and simultaneously retain the important features in practices. As mentioned in article [3], the speckle noise in medical ultrasonic images can be formulated in the following form:

$$f = u + \sqrt{n}u, \quad (2)$$

where f is a noisy image, and n represents the Gaussian random noise with zeros mean and standard deviation σ .

In this paper, we focus on the image denoising form by using variation method, where the noisy image is ultrasound speckle noise. Based on the model (2) and the characteristics of the Gaussian distribution, Krissian et al. in the article [16] derived a data fidelity term:

$$F(u, f) = \int_{\Omega} \frac{(f - u)^2}{u} dx. \quad (3)$$

Within the variational framework, the data fidelity function is derived from the degradation model (2). One of the technical approaches to solve the variational model is the regularization technique, which minimizes the cost function to obtain stable and accurate solutions. In general, the image denoising variation method is to consider:

$$\min_{u \in \Omega} E(u) = TV(u) + \lambda F(u, f), \quad (4)$$

where $TV(u)$ is a regularization term that represents a prior information about the object to be restored, and $F(u, f)$ is a fidelity term to ensure that the restoration u is not far from the original observation f . $\lambda > 0$ represents the regularization parameter which can balance the fidelity term and the regularization term.

In [11], motivated by the classical ROF model [10], the authors proposed a convex variational model for removing the speckle noise in ultrasound image. The convex variational model involves the TV regularization term and convex fidelity term (see Equation (5)):

$$\min_u \left[\int_{\Omega} |Du| dx + \lambda \int_{\Omega} \frac{(f - u)^2}{u} dx \right], \quad (5)$$

where $\int_{\Omega} |Du| dx$ represents the TV regularization term, and Du represents the directional gradient of u . The existence and uniqueness of the solution of model (5) is proved in [11]. In this paper, we call the model in (5) the “JIN’s model.” In [17], the authors proposed a well-balanced speckle noise reduction (WBSN) model that can detect edges.

Although TV regularization is effective for image denoising, it also leads to some staircase effects that is undesirable. In order to solve this problem, many methods based on improved TV regularization are proposed, such as high-order TV regularization [18–20], several hybrid TV regularization [21], the improved infimal convolution [22, 23], non-local TV model [24, 25], fractional order TV model [26], and anisotropic TV model [27, 28]. Fractional theory [29, 30], wavelet [31], and statistical information [32–34] are also employed to deal with intensity inhomogeneity or noise. Although these denoising methods can reduce the staircase effects in the restoration of additive noise images, however, there are more staircase effects that appeared in the restoration of speckle noise images. In this paper, we introduce HYPTV model and LOGTV model to reduce speckle noise and staircase effects in ultrasound images in an effective way.

In numerical algorithms, most of the energy function minimization problems can be transformed to an Euler-Lagrange equation and then be solved by using the finite difference method. However, the choice of adequate regularization terms is critical in terms of solution accuracy. Moreover, when solving the Euler-Lagrange equation, the energy diffusion form of the noise image in different regions is required to handle differently based on the physical characteristics of local coordinates, since the diffusion velocity of different parameters to the energy function is different in the two models. The new proposed HYPTV model and the LOGTV model, as shown in this paper, not only can preserve the edges of the restored images well when restoring the ultrasonic image with speckle noise but also better reduce the staircase effect generated during the recovery process.

The rest of this paper is as follows: in Section 2, we review some background knowledge. In Section 3, we propose two new models based on variation; meanwhile, we not only analyze diffusion performance of the proposed models but also give the corresponding numerical algorithms. Section 4 shows five different experiments and results. The paper ends with concluding remarks in Section 5.

2. Preliminary

2.1. Some Theoretical Background. The Euler-Lagrange equation was developed in the 1750s by Euler and Lagrange in connection with their studies of the tautochrone problem.

Theorem 1. *A multidimensional generalization comes from considering a function on m variables. If Ω is open, bounded Lipschitz domain in R^n , then*

$$A[h] = \int_{\Omega} L(x_1, x_2, \dots, x_m, h, h_1, h_2, \dots, h_m) dx, \quad (6)$$

is extremized only if h satisfies the partial differential equation:

$$\frac{\partial L}{\partial h} - \sum_{i=1}^n \frac{\partial}{\partial x_i} \left(\frac{\partial L}{\partial h_i} \right) = 0, \quad (7)$$

For model (5), the corresponding Euler-Lagrange equation is as follow:

$$\operatorname{div} \left(\frac{\nabla u}{|\nabla u|} \right) + \lambda \left(\frac{f^2}{u^2} - 1 \right) = 0, \quad (8)$$

where ∇ and div , respectively, represent gradient operators and divergence operators. Using gradient descent method, we can get the model as follows:

$$\begin{cases} u_t = \operatorname{div} \left(\frac{\nabla u}{|\nabla u|} \right) + \lambda \left(\frac{f^2}{u^2} - 1 \right), & t > 0 \quad x, y \text{ in } \Omega, \\ \frac{\partial u}{\partial \vec{n}} = 0 & \text{on the boundar of } \Omega, \\ u|_{t=0} = u_0 & \text{in } \bar{\Omega}, \end{cases} \quad (9)$$

where \vec{n} is the unit out normal vector of $\partial\Omega$.

Without losing generality, in the following, we consider the grayscale images as $M \times N$ matrices.

Definition 2. Let $u \in U = C_2^2(\Omega, R)$, $g = (g_1, g_2) \in G = C_2^2(\Omega, R^2)$, the gradient operators on the space U and the divergence operators on the space G are defined as:

$$\nabla : U \longrightarrow G, \quad \nabla u = \left(\partial_x^+ u, \partial_y^+ u \right), \quad (10)$$

$\operatorname{div} : G \longrightarrow U$, $\operatorname{div} g = \partial_x^- g_1 + \partial_y^- g_2$, where ∂_x^+ , ∂_y^+ , ∂_x^- , and ∂_y^- are the first-order forward and backward discrete derivation operators in the x -direction and y -direction, respectively, which are defined as:

$$\begin{aligned} (\partial_x^+ u) &= \begin{cases} u_{i,j+1} - u_{i,j}, & \text{if } 1 \leq j \leq N-1, \\ 0, & \text{if } j = N, \end{cases} \\ (\partial_y^+ u) &= \begin{cases} u_{i+1,j} - u_{i,j}, & \text{if } 1 \leq i \leq M-1, \\ 0, & \text{if } i = M, \end{cases} \\ (\partial_x^- u) &= \begin{cases} u_{i,j} - u_{i,j-1}, & \text{if } 2 \leq j \leq N, \\ 0, & \text{if } j = 1, \end{cases} \\ (\partial_y^- u) &= \begin{cases} u_{i,j} - u_{i-1,j}, & \text{if } 2 \leq i \leq M, \\ 0, & \text{if } i = 1. \end{cases} \end{aligned} \quad (11)$$

Applying the above gradient operators and divergence operators to model (9), we can obtain the equivalent minimization problem.

Definition 3. Let C be a convex subset of R . A function $\phi : C \longrightarrow R$ is called convex if

$$\phi(tx + (1-t)y) \leq t\phi(x) + (1-t)\phi(y), \forall x, y \in C, \forall t \in [0, 1]. \quad (12)$$

The following facts are easily checked:

Theorem 4. If functions ϕ_1 and ϕ_2 are convex and have the same domain definition, then $\phi = \phi_1 + \phi_2$ is also convex.

Proof. Let functions ϕ_1 and ϕ_2 are convex. According to the Definition 3, for any $x, y \in R$ and $t \in [0, 1]$, we have

$$\begin{aligned} \phi_1(tx + (1-t)y) &\leq t\phi_1(x) + (1-t)\phi_1(y), \\ \phi_2(tx + (1-t)y) &\leq t\phi_2(x) + (1-t)\phi_2(y), \\ \phi(tx + (1-t)y) &= \phi_1(tx + (1-t)y) + \phi_2(tx + (1-t)y) \\ &\leq t\phi_1(x) + (1-t)\phi_1(y) + t\phi_2(x) + (1-t)\phi_2(y) \\ &\leq t(\phi_1(x) + \phi_2(x)) + (1-t)(\phi_1(y) + \phi_2(y)) \\ &= t\phi(x) + (1-t)\phi(y). \end{aligned} \quad (13)$$

Hence $\phi = \phi_1 + \phi_2$ is convex.

Theorem 5. If a differentiable function $\phi : C \longrightarrow R$ satisfied

$$\phi''(x) \geq 0, \quad \forall x \in C, \quad (14)$$

then ϕ is convex.

2.2. The Condition of TV Regularization Term. Although TV regularization is very effective in image restoration, it usually generates some staircase effects. Thus, it is suggested in literature to use general variational methods, i.e., to consider:

$$J_1(u) = \int_{\Omega} \varphi(|\nabla u|) dx, \quad (15)$$

where $\varphi(s)$ represents a potential function, and the case $\varphi(s) = s$ leads to the total variation regularization term. In the literature [35], the author Costanzino chooses $\varphi(s) = s^2$ that leads to the well-known harmonic model.

In practice, we prefer good smoothing in some domain where the intensity of variations is relatively weak. This can be achieved by requiring a function $\varphi(s)$ to satisfy the following conditions:

$$\varphi'(0) = 0, \lim_{s \rightarrow 0^+} \varphi''(s) = \lim_{s \rightarrow 0^+} \frac{\varphi'(s)}{s} = c > 0. \quad (16)$$

Near the edge of the image, the intensity of variations is strong. If we would like to preserve the edge, then the function $\varphi(s)$ should satisfy the following conditions:

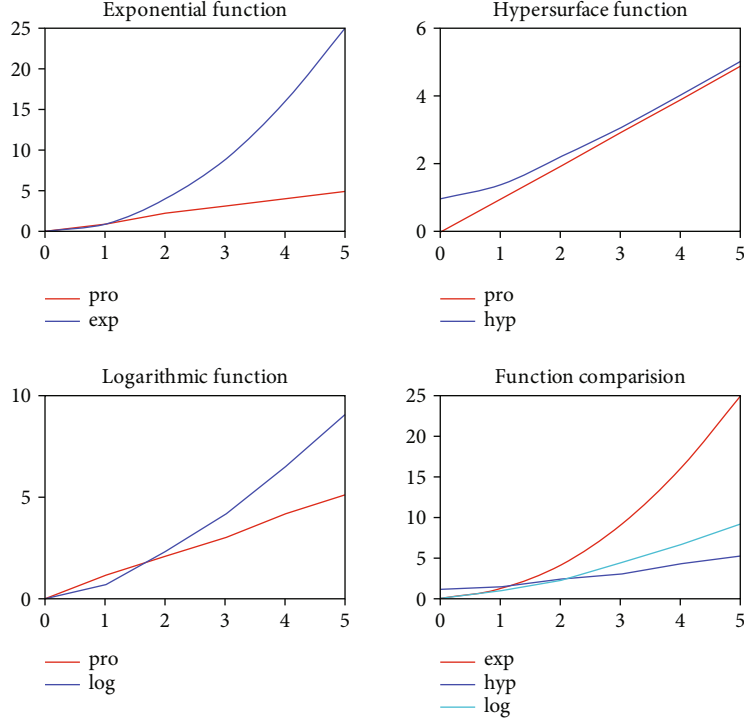


FIGURE 1: The plots of convex and nondecreasing functions.

$$\lim_{s \rightarrow \infty} \varphi''(s) = \lim_{s \rightarrow \infty} \frac{\varphi'(s)}{s} = 0, \quad \lim_{s \rightarrow \infty} \frac{s\varphi''(s)}{\varphi'(s)} = 0. \quad (17)$$

With the conditions (16) and (17), the function $\varphi(s)$ is convex and nondecreasing function, such as:

$$\begin{aligned} \text{proportional function : } \varphi(s) &= s, \quad s \geq 0, \\ \text{exponential function : } \varphi(s) &= s^2, \quad s \geq 0, \\ \text{hypersurface function : } \varphi(s) &= \sqrt{1 + \alpha_1 s^2}, \quad s \geq 0, \alpha_1 > 0, \\ \text{logarithmic function : } \varphi(s) &= s \ln(\alpha_2 + s), \quad s \geq 0, \alpha_2 > 0. \end{aligned} \quad (18)$$

These functions are convex and nondecreasing on $s \geq 0$, as shown in Figure 1.

In this paper, we will use two new functions $\varphi_1(s) = \sqrt{1 + \alpha_1 s^2}$ and $\varphi_2(s) = s \ln(\alpha_2 + s)$, which appear to be quite effective for image processing, in particular, for ultrasound image denoising. Obviously, the functions $\varphi_1(s)$ and $\varphi_2(s)$ are convex and nondecreasing.

3. The Proposed Restoration Model

In this section, we propose adaptive total variation model for image restoration. We use the finite difference method to solve the Euler-Lagrange equation directly, and then find the minimum value of the energy function.

3.1. The Adaptive Total Variation Model. Apply the selected function to model (15), we propose adaptive total variation model,

$$\min_u \left[E(u) = \int_{\Omega} \varphi_i(|\nabla u|) dx + \lambda \int_{\Omega} \frac{(f - u)^2}{u} dx \right], \quad (19)$$

where $\int_{\Omega} \varphi_i(|\nabla u|) dx$ is a regularization term, and $i = 1, 2$; $\int_{\Omega} ((f - u)^2/u) dx$ is a fidelity term; λ represents the regularization parameter which can balance fidelity term and regularization term.

Firstly, the energy functional $E(u)$ is convex, which guarantees the existence of the minimal solution of the model (19).

Theorem 6. *The energy functional $E(u)$ is convex. That is to say, for any $u_1, u_2 \in \Omega$, and $t \in [0, 1]$, we have:*

$$E(tu_1 + (1 - t)u_2) \leq tE(u_1) + (1 - t)E(u_2), \quad (20)$$

where $E(u) = \int_{\Omega} \varphi_i(|\nabla u|) dx + \lambda \int_{\Omega} ((f - u)^2/u) dx$.

Proof. Firstly, the function $\varphi_i(s)$ is convex; according to Definition 3, for any $u_1, u_2 \in \Omega$, and $t \in [0, 1]$, we have

$$\begin{aligned} \int_{\Omega} \varphi_i(|\nabla(tu_1 + (1 - t)u_2)|) dx &\leq t \int_{\Omega} \varphi_i(|\nabla u_1|) dx \\ &+ (1 - t) \int_{\Omega} \varphi_i(|\nabla u_2|) dx. \end{aligned} \quad (21)$$

Meanwhile, we have (The proof step of the inequality is in the appendix.)

$$\begin{aligned}
 \int_{\Omega} \frac{(f - (tu_1 + (1-t)u_2))^2}{tu_1 + (1-t)u_2} dx &= \int_{\Omega} \left(\frac{f^2}{tu_1 + (1-t)u_2} - 2f + tu_1 + (1-t)u_2 \right) dx \\
 &\leq \int_{\Omega} \left(\frac{f^2(tu_2 + (1-t)u_1)}{u_1 u_2} - 2f + tu_1 + (1-t)u_2 \right) dx \\
 &= \int_{\Omega} \left(\frac{tf^2}{u_1} - 2tf + tu_1 + \frac{(1-t)f^2}{u_2} - 2(1-t)f + (1-t)u_2 \right) dx \\
 &= \int_{\Omega} t \left(\frac{(f - u_1)^2}{u_1} \right) + (1-t) \left(\frac{(f - u_2)^2}{u_2} \right) dx.
 \end{aligned} \tag{22}$$

Therefore,

$$E(tu_1 + (1-t)u_2) \leq tE(u_1) + (1-t)E(u_2). \tag{23}$$

This proof is established.

Secondly, the uniqueness of the minimum solution of the model (19) can also be proved.

Theorem 7. If u_1 and u_2 are two minimize solutions of model (19), then we have $u_1 = u_2$.

Proof. According to Theorem 6, we have

$$\begin{aligned}
 E\left(\frac{u_1 + u_2}{2}\right) &= \int_{\Omega} \varphi_i \left(\left| \nabla \left(\frac{1}{2}u_1 + \frac{1}{2}u_2 \right) \right| \right) dx \\
 &\quad + \lambda \int_{\Omega} \frac{(f - ((u_1/2) + (u_2/2)))^2}{u_1 + u_2/2} dx \\
 &\leq \int_{\Omega} \left(\frac{1}{2} \varphi_i(|\nabla u_1|) + \frac{1}{2} \varphi_i(|\nabla u_2|) \right) dx \\
 &\quad + \lambda \int_{\Omega} \left(\frac{f^2(1/4(u_1 + u_2)^2 - 1/4(u_1 - u_2)^2)}{(1/2u_1 + 1/2u_2)u_1 u_2} \right. \\
 &\quad \left. - 2f + \frac{1}{2}u_1 + \frac{1}{2}u_2 \right) dx \\
 &\leq \frac{1}{2} \int_{\Omega} \varphi_i(|\nabla u_1|) dx + \frac{1}{2} \int_{\Omega} \varphi_i(|\nabla u_2|) dx \\
 &\quad + \lambda \int_{\Omega} \left(\frac{(f - u_1)^2}{2u_1} + \frac{(f - u_2)^2}{2u_2} - \frac{f^2(u_1 - u_2)^2}{2(u_1 + u_2)u_1 u_2} \right) dx \\
 &= \frac{1}{2}E(u_1) + \frac{1}{2}E(u_2) - \lambda \int_{\Omega} \frac{f^2(u_1 - u_2)^2}{2(u_1 + u_2)u_1 u_2} dx \\
 &= E(u_1) - \lambda \int_{\Omega} \frac{f^2(u_1 - u_2)^2}{2(u_1 + u_2)u_1 u_2} dx.
 \end{aligned} \tag{24}$$

If $u_1 \neq u_2$, then the above assumption gives a contradiction that u_1 is not a minimize solution.

3.2. Diffusion Performance. In this subsection, we mainly analyze the diffusion performance and diffusion speed of the energy function of HYPTV model and LOGTV model.

3.2.1. Diffusion Performance of HYPTV Model. Firstly, we use the finite difference method to solve the HYPTV model, associated with the potential function $\varphi_1(s) = \sqrt{1 + \alpha_1 s^2}$.

From Definition 2, we can obtain the corresponding Euler-Lagrange equation HYPTV model that as follows:

$$\operatorname{div} \left[\left(\frac{\alpha_1}{\sqrt{1 + \alpha_1 |\nabla u|^2}} \right) \nabla u \right] + \lambda \left(\frac{f^2}{u^2} - 1 \right) = 0. \tag{25}$$

Using gradient descent method, Equation (25) can be transformed to:

$$\begin{cases} u_t = \operatorname{div} \left[\left(\frac{\alpha_1}{\sqrt{1 + \alpha_1 |\nabla u|^2}} \right) \nabla u \right] + \lambda \left(\frac{f^2}{u^2} - 1 \right) & \text{in } \Omega, \\ \frac{\partial u}{\partial \vec{n}} = 0 & \text{on the boundar of } \Omega, \\ u|_{t=0} = u_0 & \text{in } \bar{\Omega}, \end{cases} \tag{26}$$

where \vec{n} is the unit out normal vector of $\partial\Omega$.

In order to analyze the diffusion performance, local image coordinate system ξ - η is established. As shown in Figure 2, the η -axis represents the direction parallel to the image gradient at the pixel level, and the ξ -axis is the corresponding vertical direction.

According to Figure 2, we can know:

$$\begin{cases} \xi = \frac{1}{|\nabla u|} (-u_y, u_x), \\ \eta = \frac{1}{|\nabla u|} (u_x, u_y). \end{cases} \tag{27}$$

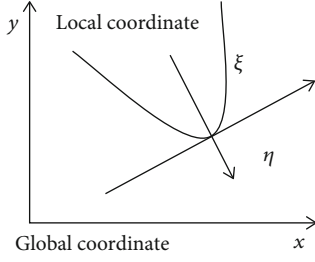


FIGURE 2: Global and local coordinate schematic diagram.

So, Equation (26) can be rewritten as:

$$u_t = \psi_1^1(|\nabla u|)u_{\xi\xi} + \psi_2^1(|\nabla u|)u_{\eta\eta} + \lambda\left(\frac{f^2}{u^2} - 1\right), \quad (28)$$

where

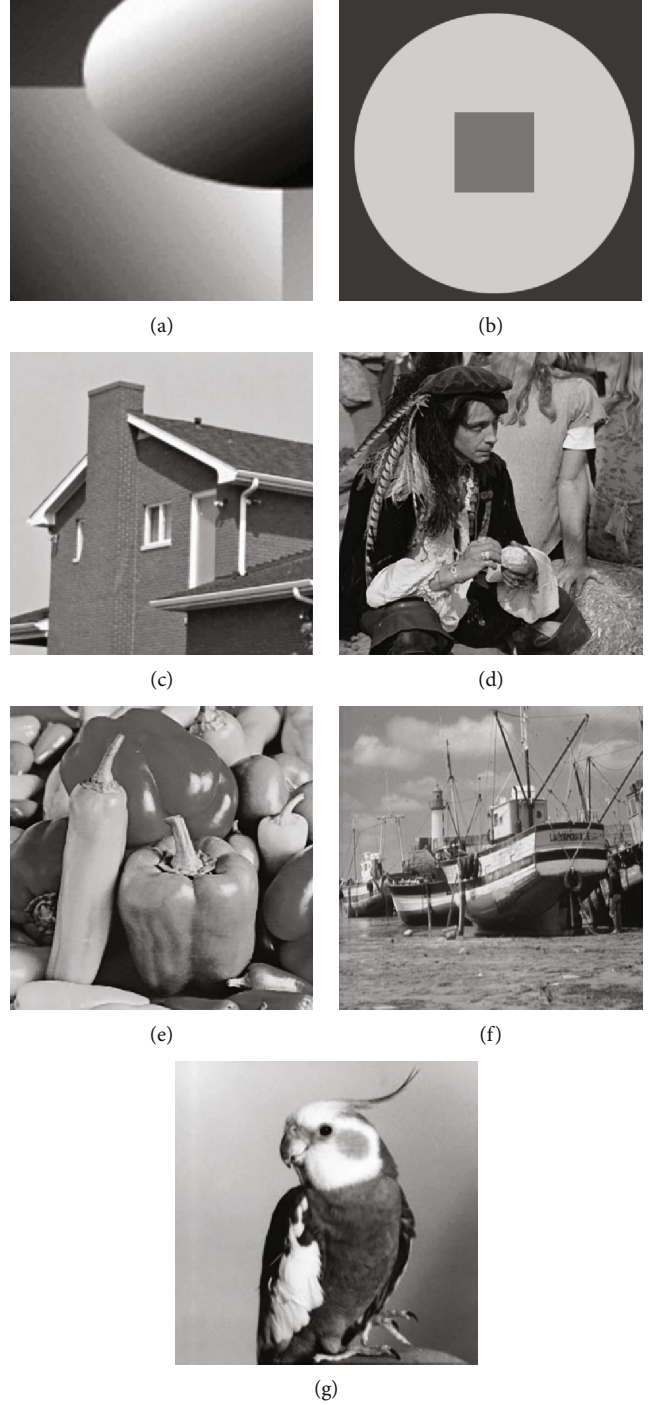
$$\begin{cases} \psi_1^1(|\nabla u|) = \frac{\alpha_1}{\sqrt{(1 + \alpha_1|\nabla u|^2)}}, \\ \psi_2^1(|\nabla u|) = \frac{\alpha_1}{(1 + \alpha_1|\nabla u|^2)^{3/2}}, \\ u_{\xi\xi} = \frac{u_y^2 u_{xx} - 2u_x u_y u_{xy} + u_x^2 u_{yy}}{|\nabla u|^2}, \\ u_{\eta\eta} = \frac{u_x^2 u_{xx} + 2u_x u_y u_{xy} + u_y^2 u_{yy}}{|\nabla u|^2}. \end{cases} \quad (29)$$

The $\psi_1^1(|\nabla u|)$ and $\psi_2^1(|\nabla u|)$ are control functions of the diffusion along the ξ -direction and η -direction, respectively. Now, we consider the diffusion of image restoration. Some test images are shown in Figure 3.

(1) *Smooth area.* When $|\nabla u| \rightarrow 0$, $\lim_{|\nabla u| \rightarrow 0} \psi_1^1(|\nabla u|) = \lim_{|\nabla u| \rightarrow 0} \psi_2^1(|\nabla u|) = \alpha_1$. This shows that the diffusion form of the energy Equation (19) is isotropic. In other words, the energy diffusion rate along direction ξ and direction η is very close in the process of image restoration in the smooth region. And the rate of energy diffusion is obviously positively correlated with the parameter α_1 .

(2) *Sharp area.* When $|\nabla u| \rightarrow \infty$, we obtain $\lim_{|\nabla u| \rightarrow \infty} (\psi_2^1(|\nabla u|)/\psi_1^1(|\nabla u|)) = 0$. This shows that the diffusion form of the energy Equation (19) is anisotropic. In other words, the energy diffusion rate in ξ -direction in Equation (28) is much larger than that in the η -direction in the sharp region. But the gradient $|\nabla u|$ does not exceed 255, so $\lim_{|\nabla u| \rightarrow 255} (\psi_2^1(|\nabla u|)/\psi_1^1(|\nabla u|)) = \lim_{|\nabla u| \rightarrow 255} (1/\sqrt{1 + \alpha_1|\nabla u|^2}) = 1/\sqrt{1 + \alpha_1 \times 255^2}$.

One can see that the larger the parameter α_1 is set, the smaller

FIGURE 3: Test images: (a) image 1 (256×256); (b) image 2 (256×256); (c) house (256×256); (d) pirate (512×512); (e) peppers (256×256); (f) boat (512×512); (g) bird (256×256).

the limit becomes. And the rate of energy diffusion is obviously positively correlated with the parameter α_1 .

3.2.2. Diffusion Performance of LOGTV Model. Secondly, we use the finite difference method to solve the LOGTV model, which the potential function is $\phi_2(s) = s \ln(\alpha_2 + s)$.

```

1:Initialize  $\lambda^0 = 0, u^0 = f, k = 0$ 
2:Repeat
3:While  $NDR > \text{limit}$  do
4:  Update  $u_k$  by (35)
5:  Update  $\lambda_k$  by (39)
6:  Computer NDR
7:  Set  $k = k + 1$ 
8: End While
9: Final Input:  $u$ 

```

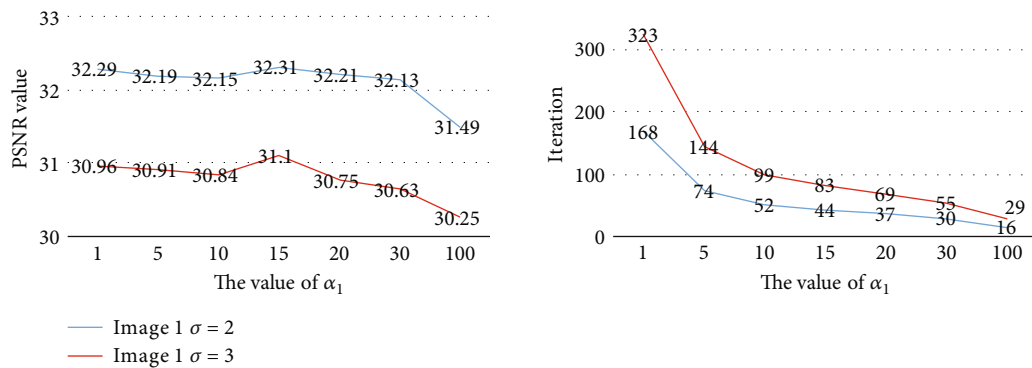
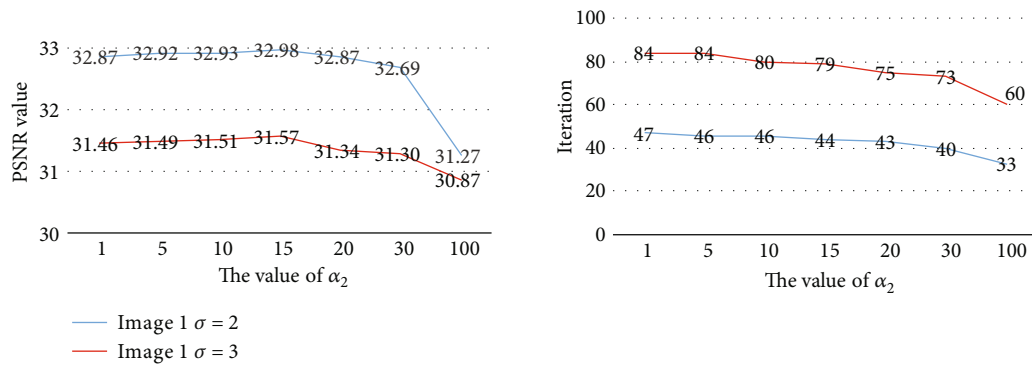
ALGORITHM 1

```

1:Initialize  $\lambda^0 = 0, u^0 = f, k = 0$ 
2:Repeat
3:While  $NDR > \text{limit}$  do
4:  Update  $u_k$  by (41)
5:  Update  $\lambda_k$  by (43)
6:  Computer NDR
7:  Set  $k = k + 1$ 
8: End While
9: Final Input:  $u$ 

```

ALGORITHM 2

FIGURE 4: The PSNR values and iteration times of different parameter α_2 (HYPTV model).FIGURE 5: The PSNR values and iteration times of different parameter α_2 (LOGTV model).

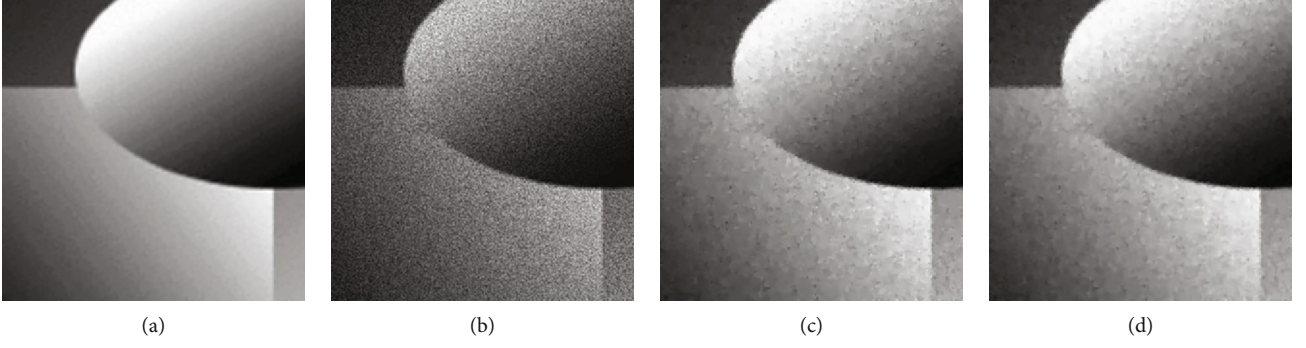


FIGURE 6: Numerical result of the “image 1” image with noise standard deviation $\sigma = 2$. (a) Original image (image 1); (b) noisy image; (c) restored image by HYPTV model $\alpha_1 = 15$; (d) restored image by LOGTV model $\alpha_2 = 15$.

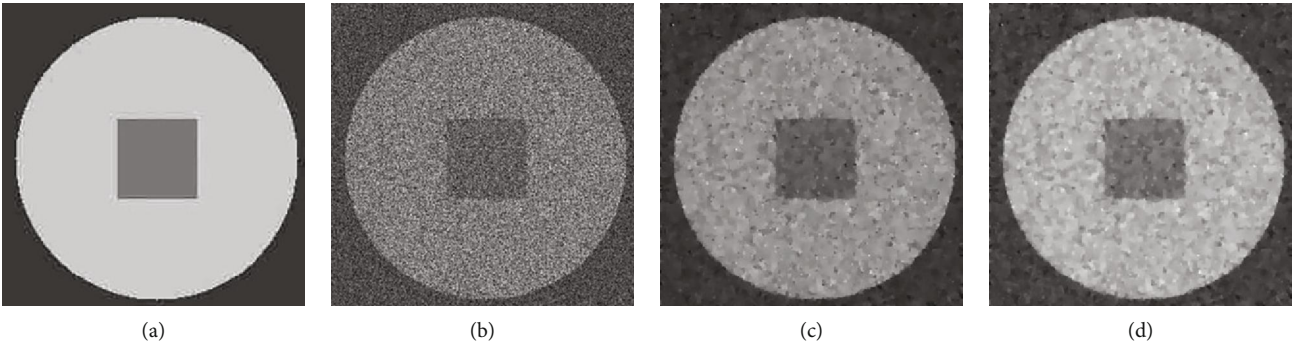


FIGURE 7: Numerical result of the “image 2” image with noise standard deviation $\sigma = 3$. (a) Original image (image 2); (b) noisy image; (c) restored image by HYPTV model $\alpha_1 = 15$; (d) restored image by LOGTV model $\alpha_2 = 15$.

TABLE 1: Numerical result of the “image 1” and “image 2” images by the HYPTV and LOGTV model.

Image	σ	Noise image PSNR	HYPTV (PSNR/SSIM)	LOGTV (PSNR/SSIM)
Image 1	2	23.76	32.31/0.7786	32.98/0.8025
Image 2	2	23.26	34.78/0.8360	35.31/0.8562
Image 1	3	20.24	31.10/0.7806	31.57/0.7948
Image 2	3	19.76	33.47/0.8300	34.07/0.8568
Image 1	4	17.77	29.97/0.7920	30.45/0.8113
Image 2	4	17.51	32.51/0.8649	32.63/0.8667

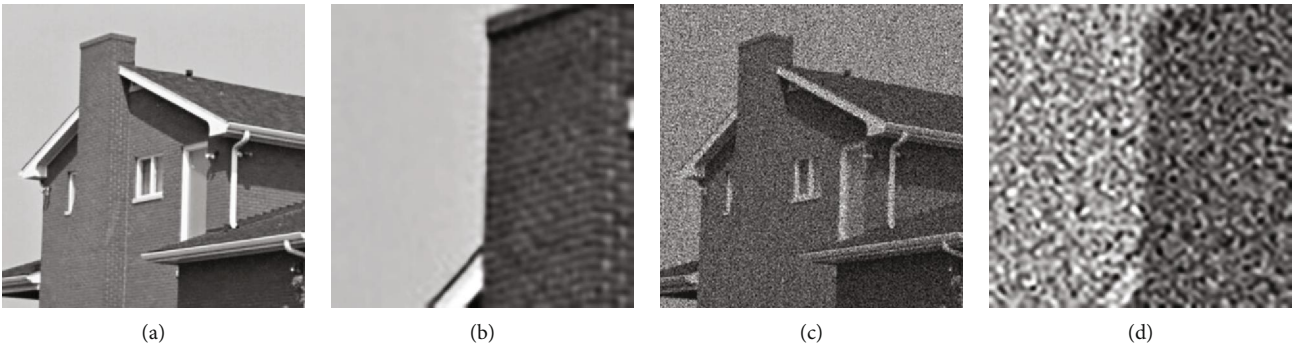


FIGURE 8: Numerical result of the “lena” and “house” images with noise standard deviation $\sigma = 3$. (a) Original images (house); (b) about the detailed image of (a); (c) noisy images; (d) about the detailed image of (c).

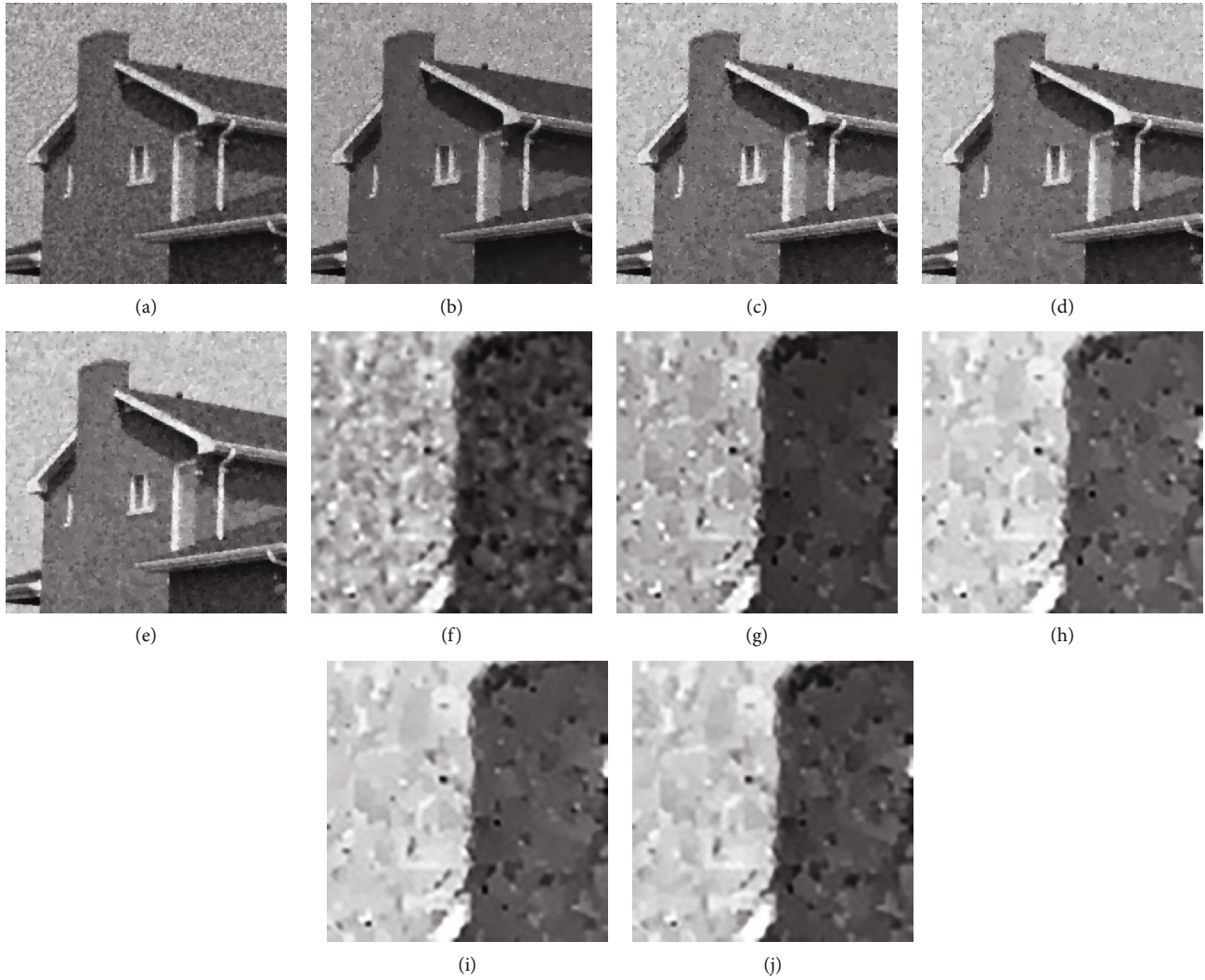


FIGURE 9: Numerical result of the “house” images with noise standard deviation $\sigma = 3$. (a) Restored image by the ROF model; (b) restored image by the ATV model; (c) restored image by the JIN’s model; (d) restored image by HYPTV model; (e) restored image by LOGTV model; (f), (g), (h), (i), and (j) about the detailed image of (a), (b), (c), (d), and (e), respectively.

From the Definition 2, we can obtain the corresponding Euler-Lagrange equation LOGTV model that as follows:

$$\operatorname{div} \left[\left(\frac{\ln(\alpha_2 + |\nabla u|)}{|\nabla u|} + \frac{1}{\alpha_2 + |\nabla u|} \right) \nabla u \right] + \lambda \left(\frac{f^2}{u^2} - 1 \right) = 0. \quad (30)$$

Using gradient descent method, Equation (30) can be transformed to:

$$u_t = \operatorname{div} \left[\left(\frac{\ln(\alpha_2 + |\nabla u|)}{|\nabla u|} + \frac{1}{\alpha_2 + |\nabla u|} \right) \nabla u \right] + \alpha \left(\frac{f^2}{u^2} - 1 \right), \quad (31)$$

where \vec{n} is the unit out normal vector of $\partial\Omega$.

Hence, Equation (31) can be rewritten as:

$$u_t = \psi_1^2(|\nabla u|) u_{\xi\xi} + \psi_2^2(|\nabla u|) u_{\eta\eta} + \lambda \left(\frac{f^2}{u^2} - 1 \right), \quad (32)$$

where

$$\begin{cases} \psi_1^2(|\nabla u|) = \frac{\ln(\alpha_2 + |\nabla u|)}{|\nabla u|} + \frac{1}{\alpha_2 + |\nabla u|}, \\ \psi_2^2(|\nabla u|) = \frac{1}{\alpha_2 + |\nabla u|} + \frac{\alpha_2}{(\alpha_2 + |\nabla u|)^2}. \end{cases} \quad (33)$$

$\psi_1^2(|\nabla u|)$ and $\psi_2^2(|\nabla u|)$ are control functions of the diffusion along the ξ -direction and η -direction, respectively. Now, we consider the diffusion of image restoration.

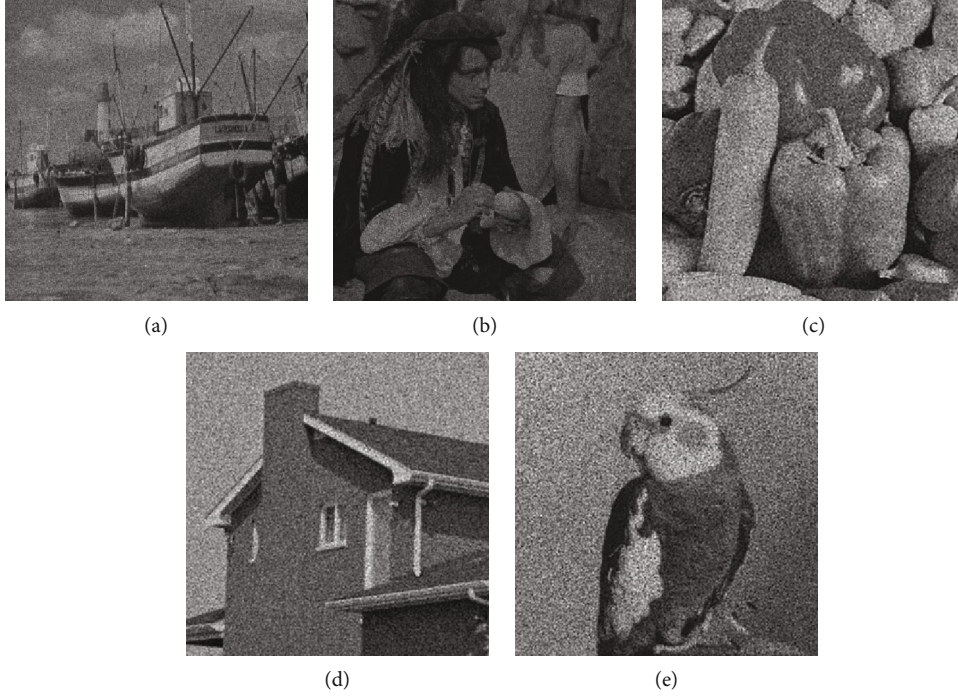


FIGURE 10: Noisy images. (a) Boat ($\sigma = 3$); (b) pirate ($\sigma = 4$); (c) peppers ($\sigma = 2$); (d) house ($\sigma = 3$); (e) bird ($\sigma = 4$).

(1) *Smooth area.* When $\alpha_2 = 1$, and $|\nabla u| \rightarrow 0$, we can obtain $\lim_{|\nabla u| \rightarrow 0} \psi_1^2(|\nabla u|) = 2$ and $\lim_{|\nabla u| \rightarrow 0} \psi_2^2(|\nabla u|) = 2$. This shows that the diffusion form of the energy Equation (19) is isotropic. In other words, the energy diffusion rate along direction ξ and direction η is very close in the process of image restoration in the smooth region. When $\alpha_2 \neq 1$, and $|\nabla u| \rightarrow 0$, we can obtain $\lim_{|\nabla u| \rightarrow 0} \psi_1(|\nabla u|) = \infty$ and $\lim_{|\nabla u| \rightarrow 0} \psi_2(|\nabla u|) = 2/\alpha_2$. This shows that the diffusion form of the energy Equation (19) is anisotropic. However, the gradient of noise image is relatively large, so in the smooth region, whatever the value of α_2 , it has little effect on the model.

(2) *Sharp area.* When $|\nabla u| \rightarrow \infty$, we can obtain $\lim_{|\nabla u| \rightarrow \infty} (\psi_1^2(|\nabla u|)/\psi_1^2(|\nabla u|)) = 0$. This shows that the diffusion form of the energy Equation (19) is anisotropic. In other words, the energy diffusion rate in ξ -direction in Equation (28) is much larger than that in the η -direction in the sharp region. But the gradient $|\nabla u|$ does not exceed 255, so $\lim_{|\nabla u| \rightarrow 255} (\psi_2(|\nabla u|)/\psi_1(|\nabla u|)) = (510\alpha_2 + 255^2)/(225\alpha_2 + 255^2 + (\alpha_2 + 255)^2 * \ln(\alpha_2 + 255))$. One can see that the larger the parameter α_2 is set, the smaller the limit becomes. And the rate of energy diffusion is clearly positively correlated with the parameter α_2 .

3.3. Numerical Implementation. We will describe the corresponding numerical algorithm in this section. Firstly, the HYPTV model can be solved by discretization as follows:

$$u_{i,j}^{k+1} = u_{i,j}^k + \Delta t \left[\operatorname{div} \left(T_1(|\nabla u^k|) \nabla u^k \right)_{i,j} + \lambda^k \left(\frac{f^2}{(u^k)^2} - 1 \right)_{i,j} \right], \quad (34)$$

where $T_1(|\nabla u^k|) = \alpha_1 / \sqrt{1 + \alpha_1 |\nabla u^k|^2}$, and Δt represents time step. Furthermore, the iterative formula can approximate as:

$$u_{i,j}^{k+1} = u_{i,j}^k + \Delta t \left[A_1(\nabla u^k)_{i,j} + \lambda^k \left(\frac{f^2}{(u^k)^2} - 1 \right)_{i,j} \right], \quad (35)$$

for $i = 1, \dots, M$; $j = 1, \dots, N$, and $M \times N$ represent the size of the image. Here:

$$A_1(\nabla u^k)_{i,j} = \partial_x^- \left(T_1(|\nabla_x u^k|) \partial_x^+ u^k \right)_{i,j} + \partial_y^- \left(T_1(|\nabla_y u^k|) \partial_y^+ u^k \right)_{i,j},$$

$$\begin{cases} |\nabla_x(u_{i,j})| = \sqrt{(\partial_x^+(u_{i,j}))^2 + (m[\partial_y^+(u_{i,j}), \partial_y^-(u_{i,j})])^2} + \delta, \\ |\nabla_y(u_{i,j})| = \sqrt{(\partial_y^+(u_{i,j}))^2 + (m[\partial_x^+(u_{i,j}), \partial_x^-(u_{i,j})])^2} + \delta, \end{cases} \quad (36)$$

where $m[a, b] = ((\operatorname{sign} a + \operatorname{sign} b)/2) \cdot \min(|a|, |b|)$, and $\delta > 0$ is a positive parameter that is close to zero. With boundary conditions:

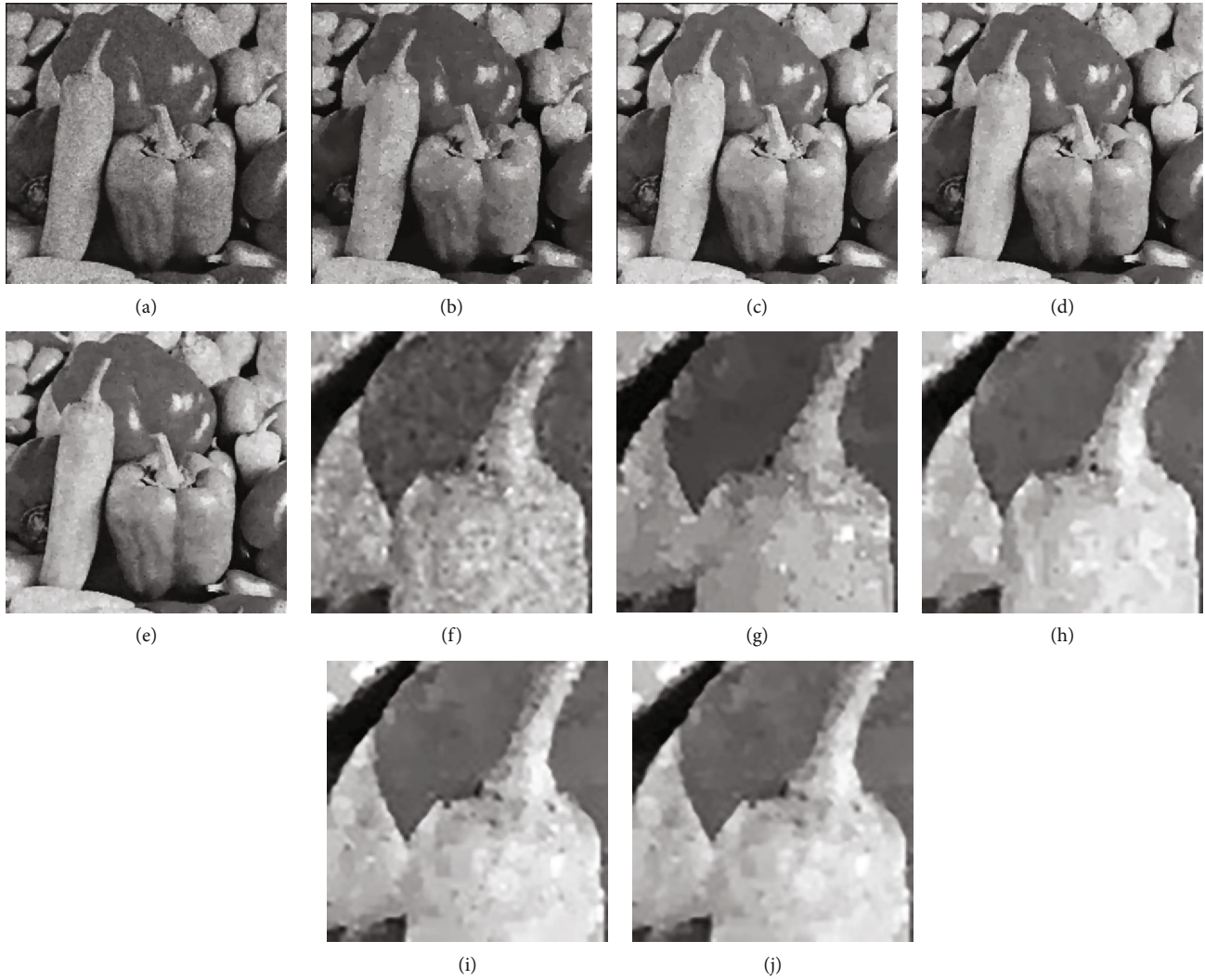


FIGURE 11: Numerical result of the “peppers” image with noise standard deviation $\sigma = 2$; (a) restored image by the ROF model; (b) restored image by the ATV model; (c) restored image by the JIN’s model; (d) restored image by HYPTV model; (e) restored image by LOGTV model; (f), (g), (h), (i), and (j) about the detailed image of (a), (b), (c), (d) and (e), respectively.

$$\begin{cases} u_{0,j}^k = u_{1,j}^k; & u_{N+1,j}^k = u_{N,j}^k, \\ u_{i,0}^k = u_{i,1}^k; & u_{i,N+1}^k = u_{i,N}^k. \end{cases} \quad (37)$$

Now, note Equation (25), the two sides are multiplied by $(f - u)u/f + u$, and then, the integral on the domain Ω can be obtained:

$$\lambda \int_{\Omega} \frac{(f - u)^2}{u} = \int_{\Omega} \operatorname{div} \left[\left(\frac{\alpha_1}{\sqrt{1 + \alpha_1 |\nabla u|^2}} \right) \nabla u \right] \frac{(u - f)u}{u + f}, \quad (38)$$

Because the Gaussian noise n have mean 0 and variance σ^2 , we can obtain:

$$\lambda^k = \frac{1}{\sigma^2 |\Omega|} \sum_{i,j} \left(A_1(\nabla u^k) \right) \frac{(u^k - f)u^k}{u^k + f}, \quad (39)$$

In the process of iteration, we always use the previous solution to calculate the next solution. The optimization algorithm for HYPTV model is given in the following (Algorithm 1).

Secondly, the LOGTV model can be solve by discretization as follows:

$$u_{i,j}^{k+1} = u_{i,j}^k + \Delta t \left[\operatorname{div} \left(T_2(|\nabla u^k|) \nabla u^k \right)_{i,j} + \lambda^k \left(\frac{f^2}{(u^k)^2} - 1 \right)_{i,j} \right], \quad (40)$$

where $T_2(|\nabla u^k|) = ((\ln(\alpha_2 + |\nabla u^k|))/|\nabla u^k|) + (1/(\alpha_2 + |\nabla u^k|))$. Furthermore, the iterative formula can approximate as:



FIGURE 12: Numerical result of the “boat” image with noise standard deviation $\sigma = 3$. (a) Restored image by the ROF model; (b) restored image by the ATV model; (c) restored image by the JIN’s model; (d) restored image by HYPTV model; (e) restored image by LOGTV model; (f), (g), (h), (i), and (j) about the detailed image of (a), (b), (c), (d), and (e), respectively.

$$u_{i,j}^{k+1} = u_{i,j}^k + \Delta t \left[A_2 \left(\nabla u^k \right)_{i,j} + \lambda^k \left(\frac{f^2}{(u^k)^2} - 1 \right)_{i,j} \right], \quad (41)$$

$$A_2 \left(\nabla u^k \right)_{i,j} = \partial_x^- \left(T_2 \left(\left| \nabla_x^+ u^k \right| \right) \partial_x^+ u^k \right)_{i,j} + \partial_y^- \left(T_2 \left(\left| \nabla_y^+ u^k \right| \right) \partial_y^+ u^k \right)_{i,j}, \quad (42)$$

$$\lambda^k = \frac{1}{\sigma^2 |\Omega|} \sum_{i,j} \left(A_2 \left(\nabla u^k \right) \right) \frac{(u^k - f)}{u^k + f}. \quad (43)$$

Similar to the HYPTV model, the optimization algorithm for LOGTV model is given in the following (Algorithm 2).

4. Experimental Results

In this section, we present numerical results to demonstrate the effectiveness of the HYPTV and LOGTV model

in image restoration. Firstly, to evaluate the quality of restored images, we use the peak signal-to-noise ratio (PSNR) value and the structure similarity (SSIM) index, which are defined as follows:

$$\text{PSNR}(u, \bar{u}) = 10 \log_{10} \left(\frac{255^2 mn}{\|u - \bar{u}\|_2^2} \right), \quad (44)$$

$$\text{SSIM}(u, \bar{u}) = \frac{(2\mu_u \mu_{\bar{u}} + c_1)(\sigma_{\bar{u}u} + c_2)}{(\mu_u^2 + \mu_{\bar{u}}^2 + c_1)(\sigma_u^2 + \sigma_{\bar{u}}^2 + c_2)},$$

where $u \in \mathbb{R}^{m \times n}$ is the clean image, and $\bar{u} \in \mathbb{R}^{m \times n}$ is the restored image. μ_a is the average of a , σ_a is the standard deviation of a , and c_1 and c_2 are some constants for stability. Secondly, we calculated the noise deviation reduction (NDR) at each iteration as a convergence condition;

$$\text{NDR} = \text{mean} \frac{(f - u_k)^2}{u_k}, \quad (45)$$

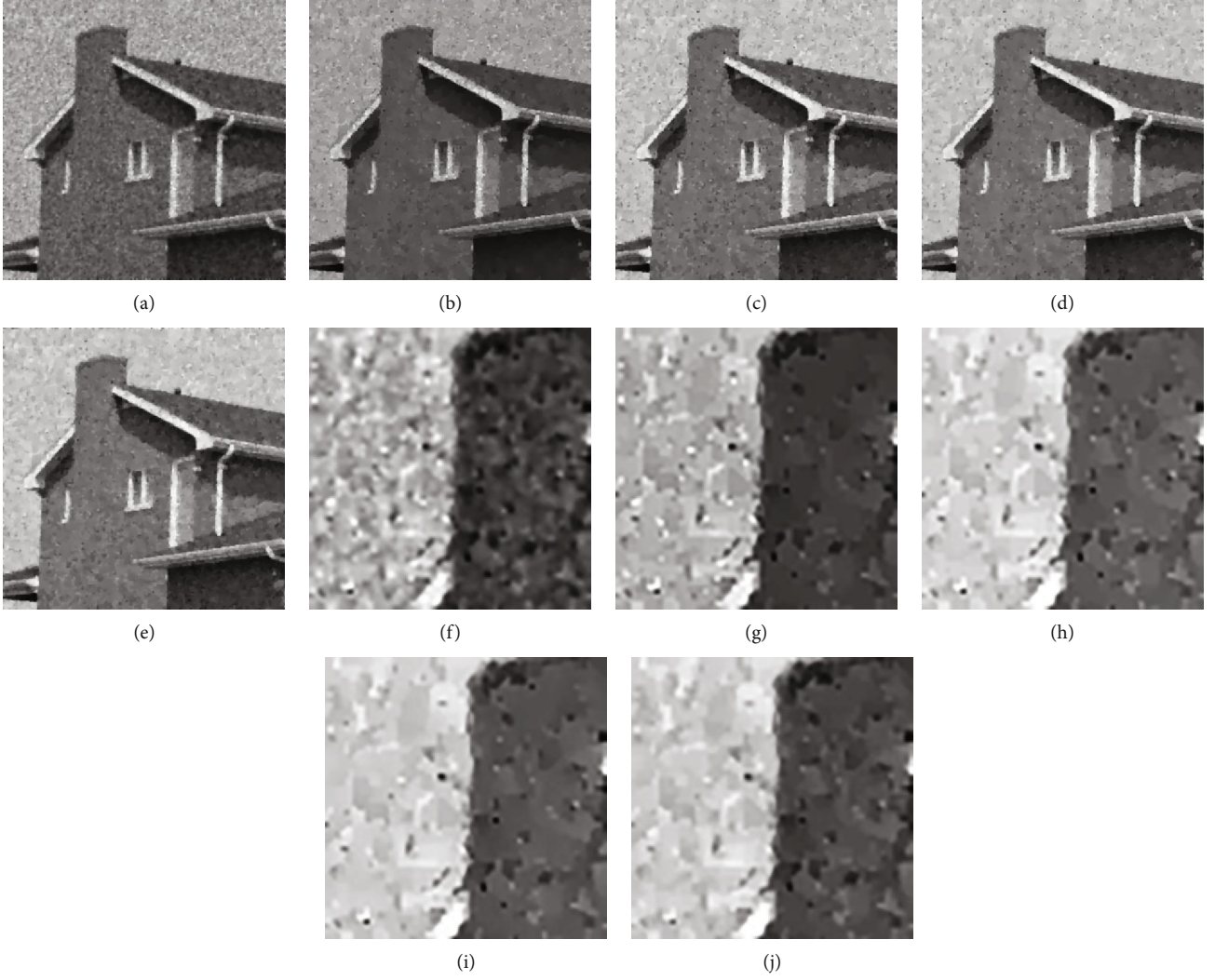


FIGURE 13: Numerical result of the “house” image with noise standard deviation $\sigma = 3$. (a) Restored image by the ROF model; (b) restored image by the ATV model; (c) restored image by the JIN’s model; (d) restored image by HYPTV model; (e) restored image by LOGTV model; (f), (g), (h), (i), and (j) about the detailed image of (a), (b), (c), (d), and (e), respectively.

where u_k represents the results of the k th iterations, respectively. Finally, the stopping condition (NDR) for the HYPTV and LOGTV models is as follows:

$$\left| \sqrt{\text{NDR}} - \sigma \right| \leq 10^{-1}, \quad (46)$$

In the numerical experiment, we will use the noise image as the initial value, that is, $f = u_0$. Moreover, the gray values of all original images are in range $[0, 255]$.

4.1. Denoising Effect of Different Parameters of HYPTV Model and LOGTV Model. In this example, we use different parameter $\alpha_i (i = 1, 2)$ values in the algorithm to test the effect of HYPTV and LOGTV models. The test images is shown in Figure 3(a), and the noise levels are $\sigma = 2$ and $\sigma = 3$. Figure 4 shows the different PSNR values and iteration numbers when different β values are used in the HYPTV model algorithm. Figure 5 shows the different PSNR values and iteration numbers when different β values are used in the

LOGTV model algorithm. Firstly, we can also see that PSNR is the largest in $\alpha_i (i = 1, 2) = 15$. Secondly, with the increase of parameters, the speed of image restoration is faster. Based on the above analysis, when $\alpha_i (i = 1, 2) = 15$, the denoising performance of HPYTV and LOGTV models is close to the best. Therefore, in the following experiment, we choose $\alpha_i (i = 1, 2) = 15$ in HPYTV and LOGTV models.

4.2. Denoising Effect of the HYPTV and LOGTV Model. In this subsection, we use the algorithm to test the effect of the HYPTV and LOGTV model on image denoising. In Figures 6 and 7, we show the original images, the noise images, and the restored images by HYPTV and LOGTV models. Figures 6(a) and 7(a) are original images, Figures 6(b) and 7(b) are noisy images, which the noise levels are $\sigma = 2$ and $\sigma = 3$, respectively. Figures 6(c) and 7(c) are corresponding restored images by HYPTV model. Figures 6(d) and 7(d) are corresponding restored images by LOGTV model. Table 1 shows that the PSNR values, SSIM values, and the numbers of iteration for the different test



FIGURE 14: Numerical result of the “pirate” image with noise standard deviation $\sigma = 4$. (a) Restored image by the ROF model; (b) restored image by the ATV model; (c) restored image by the JIN’s model; (d) restored image by HYPTV model; (e) restored image by LOGTV model; (f), (g), (h), (i), and (j) about the detailed image of (a), (b), (c), (d), and (e), respectively.

images can be got by using the HYPTV model and the LOGTV model. “Noise image PSNR” is the peak signal-to-noise ratio of noisy images and original images. “Denoising image PSNR” is the peak signal-to-noise ratio of restored images and original images. “Iter” is the number of iterations of the algorithm. From the results, it is obvious that the HYPTV model and the LOGTV model are fairly effective in reducing the speckle noise and edge-preserving.

4.3. Reduction of Staircase. In this subsection, we test the reduction of the staircase effect in HYPTV model and LOGTV model by image in Figure 8. Figure 8(a) shows original images (“house”). Figure 8(b) shows detailed images of Figure 8(a), respectively. Figure 8(c) shows noise images which noise standard deviation $\sigma = 3$. Figure 8(d) shows detailed images of Figure 8(c). The original images contain a lot of details information, such as textures edges and in homogeneous regions.

Figure 9 displays the restoration results of the noisy “house” image, respectively. Figures 9(a)–9(e) was restored ROF model [10], ATV model [36], JIN’s model [11], HYPTV model, and LOGTV model, respectively. Figures 9(f)–9(j) is corresponding details images.

According to the results, we can see that JIN’s model, HYPTV model, and LOGTV model had a good effect in removing image noise and preserving image edges. In addition, we can clearly see staircase effect in the detailed images obtained by ROF model, ATV model, and JIN’s model. At the same time, the staircase effect of HYPTV model and LOGTV model restored images is reduced. Although both the HYPTV model and the LOGTV model can reduce the ladder effect, the LOGTV model is better than the HYPTV model.

4.4. Comparison with ROF Model, ATV Model, and JIN’s Model. In this subsection, we compare the effect of the ROF model, ATV model, and JIN’s model with HYPTV and LOGTV models for some images. The test original images

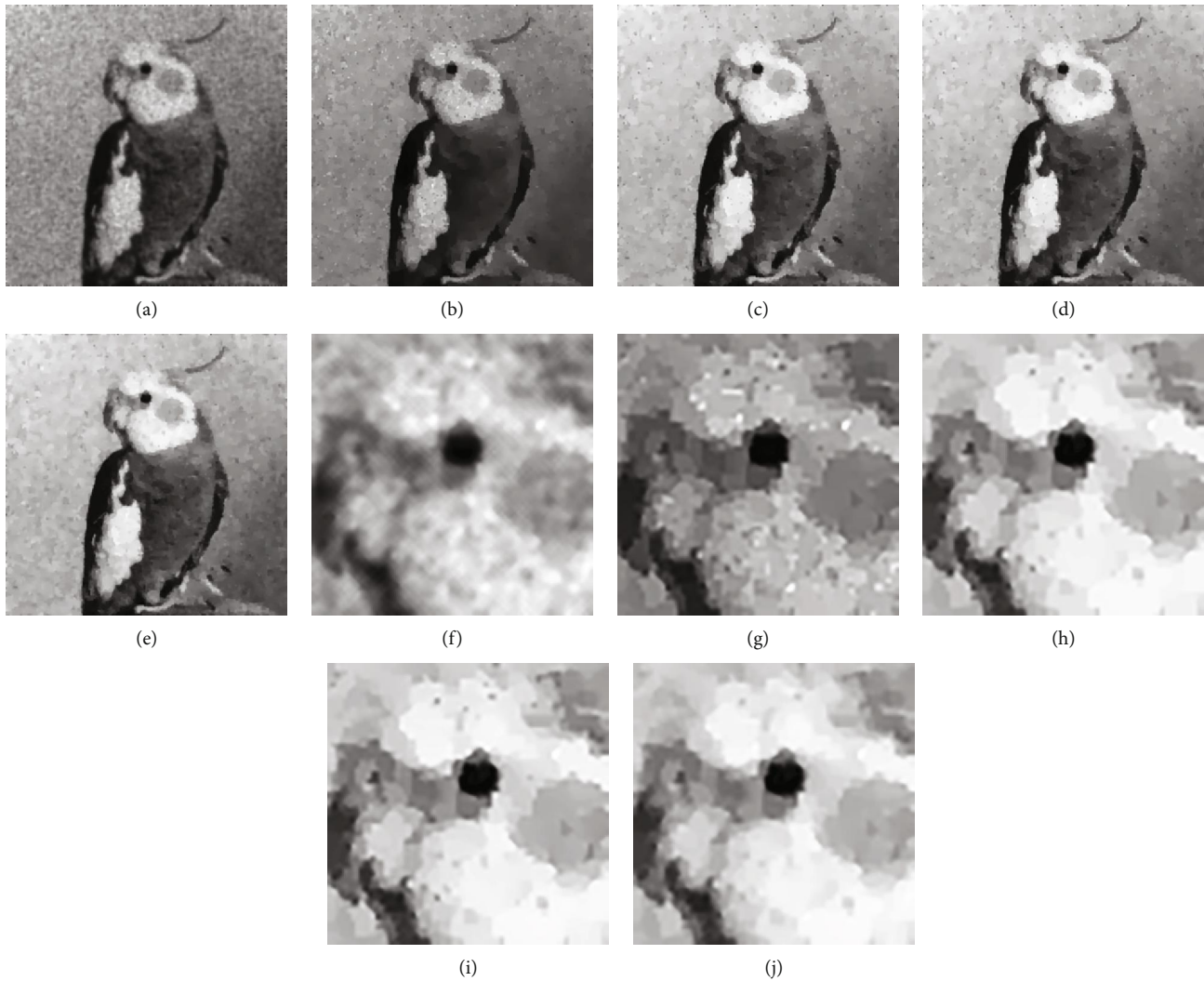


FIGURE 15: Numerical result of the “bird” image with noise standard deviation $\sigma = 4$. (a) Restored image by the ROF model; (b) restored image by the ATV model; (c) restored image by the JIN’s model; (d) restored image by HYPTV model; (e) restored image by LOGTV model; (f), (g), (h), (i), and (j) about the detailed image of (a), (b), (c), (d), and (e), respectively.

are shown in Figure 3 (“house,” “peppers,” “boat,” “pirate,” and “bird”), with two sizes of 512×512 and three sizes of 256×256 . Figure 10 shows some noise images with different standard deviation.

Figures 11–15 display the restoration results for images (“peppers,” “boat,” “house,” “pirate,” and “bird”) through ROF model, ATV model, JIN’s model, HYPTV model, and LOGTV model. The noise versions of “peppers,” “boat” and “house,” and “pirate” and “bird” are obtained by model (2) with standard deviations 2, 3, and 4, respectively. In addition, the detailed images of the restored images are also displayed. Table 2 shows the PSNR and SSIM values for different test images by using the ROF model, ATV model, JIN’s model, HYPTV model, and LOGTV model. From the results of Figures 11–15 and Table 2, the noise standard deviation $\sigma = 2$. We can observe that although the four models can effectively remove the noises while preserving the edges and details, the restored images by HYPTV model and LOGTV model have better visual effect with less staircase effects than by the ROF model,

ATV model, and JIN’s model. The noise standard deviation $\sigma = 3, 4$. The visual effect of restored images by the ROF model and ATV model is particularly poor, but JIN’s model, HYPTV model, and LOGTV model can effectively remove the noises. Finally, Table 2 shows that LOGTV model has higher PSNR and SSIM values than other four models. This means that our proposed LOGTV model is available in reducing the speckle noise in some images.

4.5. Denoising Results of Real Ultrasound Images. In this subsection, we test some real ultrasound images. Figure 16 shows the experimental results of real ultrasound images by applying JIN’s model, HYPTV model, and LOGTV model. Table 3 shows the different iteration for the different test images by using the JIN’s model, HYPTV model, and LOGTV model. We find that LOGTV model is much effective than JIN’s model and HYPTV model in obtaining the satisfactory restored images.

TABLE 2: The PSNR of the restored images by the different model.

Image	σ	ROF (PSNR/SSIM)	ATV (PSNR/SSIM)	JIN's (PSNR/SSIM)	HYPTV (PSNR/SSIM)	LOGTV (PSNR/SSIM)
Peppers	2	27.60/0.7183	28.66/0.8377	29.46/0.8195	29.43/0.8250	29.53/0.8274
Boat	2	27.26/0.8240	27.90/0.8574	28.35/0.8622	28.49/0.8659	28.64/0.8661
House	2	27.45/0.6185	29.06/0.8101	28.77/0.6876	29.55/0.7374	29.74/0.7447
Pirate	2	28.33/0.8975	27.22/0.8530	28.51/0.9042	28.55/0.9047	28.74/0.9060
Bird	2	28.99/0.6907	30.28/0.7849	30.36/0.7774	30.88/0.8137	31.07/0.8173
Peppers	3	25.93/0.6758	26.70/0.7409	27.13/0.7446	27.19/0.7492	27.37/0.7516
Boat	3	25.79/0.7481	26.47/0.7986	26.68/0.8029	26.64/0.7985	26.82/0.7989
House	3	26.08/0.5752	27.33/0.6611	27.24/0.6551	27.62/0.6866	27.82/0.6896
Pirate	3	26.35/0.8392	26.38/0.8332	26.81/0.8578	26.85/0.8580	26.98/0.8583
Bird	3	27.36/0.6451	27.92/0.6930	28.48/0.7307	28.92/0.7686	29.13/0.7701
Peppers	4	24.49/0.6153	25.59/0.7153	25.63/0.6800	25.65/0.6981	25.83/0.7011
Boat	4	24.47/0.6807	24.95/0.7338	25.24/0.7370	25.31/0.7382	25.51/0.7388
House	4	24.63/0.5130	25.30/0.5760	26.18/0.6399	26.19/0.6419	26.43/0.6437
Pirate	4	24.03/0.7652	24.33/0.7205	24.75/0.7787	25.64/0.8118	25.77/0.8159
Bird	4	25.66/0.5679	26.49/0.6584	27.25/0.7263	27.25/0.7270	27.51/0.7282

Best denoising performance are given in bold.

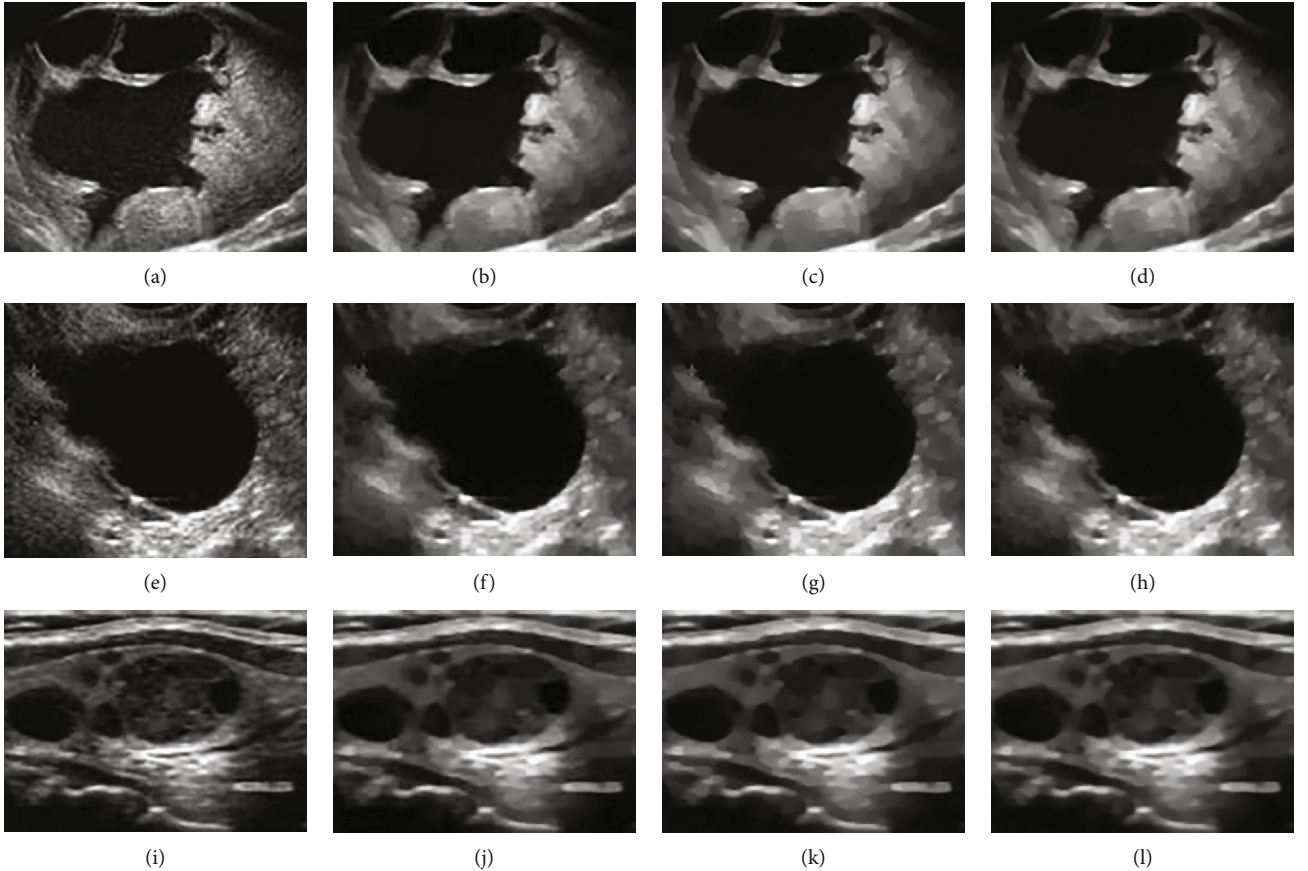


FIGURE 16: Numerical result of the real ultrasound image (the real ultrasound image from [18]). (a, e, i) Noisy image; (b, f, j) restored image by the JIN's model; (c, g, k) restored image by HYPTV model; (d, h, l) restored image by LOGTV model.

5. Concluding Remarks

In this paper, we propose a new speckle noise restoration model based on adaptive TV method. Two new convex func-

tions are introduced as the TV regularization term. By analyzing the diffusion performance of the proposed two models, one can see that the LOGTV model has faster diffusion speed than the HYPTV model. Moreover, we introduced

TABLE 3: Iteration times and time of different models.

Image	JIN's (iter/time)	HYPTV (iter/time)	LOGTV (iter/time)
Ultra 1	81/0.46 s	26/0.31 s	22/0.24 s
Ultra 2	76/0.49 s	22/0.27 s	20/0.23 s
Ultra 3	88/0.45 s	27/0.27 s	24/0.23 s

Best performance are given in bold.

two iterative numerical algorithms to solve the proposed models. The experiment results show the affectivity of our proposed model and the similarity between JIN's model and HYPTV model. In addition, we compared the effect of the ROF model, ATV model, and JIN's model with the LOGTV model, and the experiment results show high efficiency of LOGTV model in image restoration.

Appendix

The Proof of the Inequality of Theorem 6

Proof. For any $u_1, u_2 \in \Omega$, and $t \in [0, 1]$, $(tu_2 + (1-t)u_1)(tu_1 + (1-t)u_2) \geq u_1u_2$.

Here, we know $t(1-t)(u_1^2 + u_2^2) + 2t^2u_1u_2 - 2tu_1u_2 + u_1u_2 \geq u_1u_2$,

so, we have $(u_1^2 + u_2^2) \geq u_1u_2$. Therefore, the proof holds to be true.

Data Availability

The experimental data are obtained by MATLAB R2017a, 2.93 GHz cup, 4 G RAM, and Windows 7.

Conflicts of Interest

The authors declare that they have no conflicts of interest.

Authors' Contributions

All authors typed, read, and approved the final manuscript.

Acknowledgments

This paper is partially supported by the Natural Science Foundation of Guangdong Province (2018A030313364), the Special Innovation Projects of Universities in Guangdong Province (2018KTSCX197), the Science and Technology Planning Project of Shenzhen City (JCYJ20180305125609379), the Natural Science Foundation of Shenzhen (JCYJ20170818091621856), and the China Scholarship Council Project (201508440370).

References

- [1] H. H. Arsenault, "Speckle suppression and analysis for synthetic aperture radar images," *Optical Engineering*, vol. 25, no. 5, pp. 636–643, 1986.
- [2] D. Kuan, A. Sawchuk, T. Strand, and P. Chavel, "Adaptive restoration of images with speckle," *IEEE Transactions on Acoustics, Speech, and Signal Processing*, vol. 35, no. 3, pp. 373–383, 1987.
- [3] T. Loupas, W. N. McDicken, and P. L. Allan, "An adaptive weighted median filter for speckle suppression in medical ultrasonic images," *IEEE Transactions on Circuits and Systems*, vol. 36, no. 1, pp. 129–135, 1989.
- [4] Y. J. Yu and S. T. Acton, "Speckle reducing anisotropic diffusion," *IEEE Transactions on Image Processing*, vol. 11, no. 11, pp. 1260–1270, 2002.
- [5] K. Krissian, C. F. Westin, R. Kikinis, and K. G. Vosburgh, "Oriented speckle reducing anisotropic diffusion," *IEEE Transactions on Image Processing*, vol. 16, no. 5, pp. 1412–1424, 2007.
- [6] J. Shen and T. F. Chan, "Mathematical models for local non-texture inpainting," *SIAM Journal on Applied Mathematics*, vol. 62, no. 3, pp. 1019–1043, 2002.
- [7] J. Shen, S. H. Kang, and T. F. Chan, "Euler's elastica and curvature-based inpainting," *SIAM Journal on Applied Mathematics*, vol. 63, no. 2, pp. 564–592, 2003.
- [8] J. Jin, Y. Liu, Q. Wang, and S. Yi, "Ultrasonic speckle reduction based on soft thresholding in quaternion wavelet domain," in *2012 IEEE International Instrumentation and Measurement Technology Conference Proceedings*, pp. 255–262, Graz, Austria, May 2012.
- [9] M. Kang, M. Kang, and M. Jung, "Total generalized variation based denoising models for ultrasound images," *Journal of Scientific Computing*, vol. 72, no. 1, pp. 172–197, 2017.
- [10] L. I. Rudin, S. Osher, and E. Fatemi, "Nonlinear total variation based noise removal algorithms," *Physica D: Nonlinear Phenomena*, vol. 60, no. 1–4, pp. 259–268, 1992.
- [11] Z. Jin and X. Yang, "A variational model to remove the multiplicative noise in ultrasound images," *Journal of Mathematical Imaging and Vision*, vol. 39, no. 1, pp. 62–74, 2011.
- [12] K. G. Lore, A. Akintayo, and S. Sarkar, "LLNet: a deep autoencoder approach to natural low-light image enhancement," *Pattern Recognition*, vol. 61, pp. 650–662, 2017.
- [13] N. Wang, D. Tao, X. Gao, X. Li, and J. Li, "A comprehensive survey to face hallucination," *International Journal of Computer Vision*, vol. 106, no. 1, pp. 9–30, 2014.
- [14] Y. Hu, N. Wang, D. Tao, X. Gao, and X. Li, "SERF: a simple, effective, robust, and fast image super-resolver from cascaded linear regression," *IEEE Transactions on Image Processing*, vol. 25, no. 9, pp. 4091–4102, 2016.
- [15] N. Wang, X. Gao, L. Sun, and J. Li, "Bayesian face sketch synthesis," *IEEE Transactions on Image Processing*, vol. 26, no. 3, pp. 1264–1274, 2017.
- [16] K. Krissian, R. Kikinis, C. F. Westin, and K. Vosburgh, "Speckle-constrained filtering of ultrasound images," in *2005 IEEE Computer Society Conference on Computer Vision and Pattern Recognition (CVPR'05)*, pp. 547–552, San Diego, CA, USA, June 2005.
- [17] C. A. Z. Barcelos and L. E. S. R. Vieira, "Ultrasound speckle noise reduction via an adaptive edge-controlled variational method," in *2014 IEEE International Conference on Systems, Man, and Cybernetics (SMC)*, pp. 145–151, San Diego, CA, USA, October 2014.
- [18] F. Knoll, K. Bredies, T. Pock, and R. Stollberger, "Second order total generalized variation (TGV) for MRI," *Magnetic Resonance in Medicine*, vol. 65, no. 2, pp. 480–491, 2011.
- [19] M. Lysaker, A. Lundervold, and Xue-Cheng Tai, "Noise removal using fourth-order partial differential equation with applications to medical magnetic resonance images in space

- and time," *IEEE Transactions on Image Processing*, vol. 12, no. 12, pp. 1579–1590, 2003.
- [20] K. Bredies, K. Kunisch, and T. Pock, "Total generalized variation," *SIAM Journal on Imaging Sciences*, vol. 3, no. 3, pp. 492–526, 2010.
 - [21] F. Li, C. Shen, J. Fan, and C. Shen, "Image restoration combining a total variational filter and a fourth-order filter," *Journal of Visual Communication and Image Representation*, vol. 18, no. 4, pp. 322–330, 2007.
 - [22] A. Chambolle and P. L. Lions, "Image recovery via total variation minimization and related problems," *Numerische Mathematik*, vol. 76, no. 2, pp. 167–188, 1997.
 - [23] S. Setzer, G. Steidl, and T. Teuber, "Deblurring Poissonian images by split Bregman techniques," *Journal of Visual Communication and Image Representation*, vol. 21, no. 3, pp. 193–199, 2010.
 - [24] X. Liu and L. Huang, "A new nonlocal total variation regularization algorithm for image denoising," *Mathematics and Computers in Simulation*, vol. 97, no. 1, pp. 224–233, 2014.
 - [25] S. Osher, "Nonlocal operators with applications in imaging," *SIAM Journal on Multiscale Modeling and Simulation*, vol. 7, no. 3, pp. 1005–1028, 2008.
 - [26] Z. Ren, C. He, and Q. Zhang, "Fractional order total variation regularization for image super-resolution," *Signal Processing*, vol. 93, no. 9, pp. 2408–2421, 2013.
 - [27] J. S. Moll, "The anisotropic total variation flow," *Mathematische Annalen*, vol. 332, no. 1, pp. 177–218, 2005.
 - [28] H. Chen, C. Wang, Y. Song, and Z. Li, "Split Bregmanized anisotropic total variation model for image deblurring," *Journal of Visual Communication and Image Representation*, vol. 31, pp. 282–293, 2015.
 - [29] B. Chen, S. Huang, Z. Liang, W. Chen, and B. Pan, "A fractional order derivative based active contour model for inhomogeneous image segmentation," *Applied Mathematical Modelling*, vol. 65, no. 1, pp. 120–136, 2019.
 - [30] B. Chen, Q. H. Zou, W. S. Chen, and Y. Li, "A fast region-based segmentation model with Gaussian kernel of fractional order," *Adv. Math. Phys.*, vol. 2013, article 501628, 7 pages, 2013.
 - [31] B. Chen and W. S. Chen, "Noisy image segmentation based on wavelet transform and active contour model," *Applicable Analysis*, vol. 90, no. 8, pp. 1243–1255, 2010.
 - [32] B. Chen, Q. Zou, and Y. Li, "A new image segmentation model with local statistical characters based on variance minimization," *Applied Mathematical Modelling*, vol. 39, no. 12, pp. 3227–3235, 2015.
 - [33] B. Chen, Y. Li, and J. Cai, "Noisy image segmentation based on nonlinear diffusion equation model," *Applied Mathematical Modelling*, vol. 36, no. 3, pp. 1197–1208, 2012.
 - [34] B. Chen, J. L. Cai, W. S. Chen, and Y. Li, "A multiplicative noise removal approach based on partial differential equation model," *Mathematical Problems in Engineering*, vol. 2012, Article ID 242043, 14 pages, 2012.
 - [35] N. Costanzino, "Structure inpainting via variational methods," 2002, <https://www.lems.brown.edu/nc>.
 - [36] J. Fehrenbach and J. M. Mirebeau, "Sparse non-negative stencils for anisotropic diffusion," *Journal of Mathematical Imaging and Vision*, vol. 49, no. 1, pp. 123–147, 2014.